Biological Relevance of $CuFeO_2$ Nanoparticles: Antibacterial and Anti-inflammatory Activity, Genotoxicity, DNA and Protein Interactions.

O. Antonoglou[a], K. Lafazanis[b,c], S. Mourdikoudis[d,e], G. Vourlias[f], T. Lialiaris[c], A. Pantazaki[b*], C. Dendrinou-Samara[a*]

[a]Laboratory of Inorganic Chemistry, Department of Chemistry, Aristotle University of Thessaloniki, 54124 Thessaloniki, Greece.

[b]Laboratory of Biochemistry, Department of Chemistry, Aristotle University of Thessaloniki, 54124 Thessaloniki, Greece.

[c]Department of Genetics, Faculty of Medicine, Dimokrition University of Thrace, Alexandroupolis, Greece.

[d]UCL Healthcare Biomagnetic and Nanomaterials Laboratories, London, UK.

[e]Biophysics Group, Department of Physics and Astronomy, University College London (UCL), London, UK.

[f]Department of Physics, Aristotle University of Thessaloniki, 54124 Thessaloniki, Greece.

[*]Corresponding authors

E-mail address: samkat@chem.auth.gr

E-mail address: natasa@chem.auth.gr

Abstract

Heterometal oxide nanoparticles of bioessential metals are shedding new light to nanoparticle-inspired bioapplications. Pairing bioreactive elements like copper and iron can affect the redox dynamic and biological profile of the nanomaterial. Given the complexity of physicochemical properties, biological activity and toxicity concerns, extensive exploration is demanded, especially when active and less active oxidation states participate as in case of cuprous-ferric delafossite $CuFeO_2$ (copper(I)-iron(III)), a less widespread nanomaterial. In that vein, $CuFeO_2$ nanoparticles were synthesized and biological profile was evaluated in comparison with cuprous oxide (Cu_2O NPs) counterpart, an already established antimicrobial agent. Interactions with bacteria, proteins and DNA were examined. Cu_2O NPs exhibited stronger antibacterial activity (IC_{50} <25 μg/ml) than $CuFeO_2$ NPs (IC_{50}>100 μg/ml). *In vitro* exposure of nanoparticles on plasmid DNA unveiled toxicity in the form of DNA damage for Cu_2O and enhanced biocompatibility for $CuFeO_2$ NPs. Genotoxicity estimated by the frequency of sister chromatid exchanges, cytostaticity based on the proliferating rate indices and cytotoxicity based on the mitotic indices at human peripheral lymphocyte cultures were all significantly lower in the case of $CuFeO_2$ NPs. Furthermore, through *in vitro* albumin denaturation assay, $CuFeO_2$ NPs showed better performance in protein denaturation protection, correlating in superior anti-inflammatory activity than Cu_2O and similar to acetylsalicylic acid. Synergy of copper(I)-iron(III) in nanoscale is apparent and gives rise to fruitful bioapplications and perspectives.

Keywords: Delafossite; Copper(I)-Iron(III); Heterometal oxides; Sister chromatid exchange; Gel electrophoresis.

1. Introduction

The importance of nano-oxides in bioapplications is evident [1, 68]. Nanoparticles (NPs) of bioessential metals like copper and iron have attracted broad attention in diverse functions. Copper nanomaterials display an interesting and complex biological profile in multiple oxidation states (Cu, Cu_2O, CuO) as antimicrobials, agrochemicals, etc. [2, 3], while biocompatible iron oxide NPs are emerging as drug delivery platforms and imaging agents [4]. Apart from nanosize effects, bioaffinity and redox dynamics/oxidation states govern the behavior of these materials in bioapplications by affecting the equilibrium of oxidative stress, reactive oxygen species production, antioxidant activity, DNA and protein interactions, biodamage and toxicity. Recently, bimetallic and heterostructured nanomaterials are investigated in the path of optimizing various properties [5, 6, 7, 8, 9, 10, 11]. When bioessential metals participate in the structures multifarious behavior is considered and concerns for risk assessment and toxicity are complicated. Given the numerous copper-iron biorelations like linked homeostatic mechanisms and Fenton and Habber-Weiss reactions, it is challenging to unveil fruitful synergies. Our previous results on bimetallic CuFe NPs revealed enhanced antimicrobial action compared to monometallic Cu NPs attributed to increased intracellular reactive oxygen species (ROS) production [9]. Copper-iron synergy can appear in different oxidation states in heterometal oxides. Even though few reports examine such effects, the copper(II)-iron(III) pairing in copper ferrite, $CuFe_2O_4$ NPs has shown enhanced antimicrobial response [12, 13], while bioevaluation of copper(I)-iron(III) like the cuprous-ferric delafossite $CuFeO_2$ NPs is absent apart from an antiviral study by Qui et al. that showed promising results [14]. In contrast, cuprous counterpart Cu_2O NPs is already established as a potential antimicrobial agent and also commercialized [15, 16, 17, 18, 19, 20]. Generally, amongst the three oxidation states [metallic (Cu^0), cuprous (Cu^{+1}), cupric (Cu^{+2})], Cu(I) is the most reactive, being able to participate in both reductive and oxidative reactions due to similar redox potentials and has been shown to exhibit greater antimicrobial activity [14, 18, 20]. However, the higher efficiency of cuprous NPs may come with a broad biohostility and undesired toxicity that could be suppressed by the presence of a less reactive species like ferric state (Fe^{+3}). In that vein, bioevaluation of copper(I)-iron(III) would be of great interest from biocompatibility and bioreactivity perspectives.

In continuation of our research on bimetallic (copper-iron, copper-zinc) [9, 10] and heterostructured oxide (copper-nickel-iron) [21] NPs in the present work $CuFeO_2$ and Cu_2O NPs were effectively synthesized through a reduction/hydrothermal synthetic route using hydrazine hydrate. A synthetic mechanism in the sole presence of hydrazine is proposed. NPs were thoroughly characterized to determine their particle size, morphology, structure, composition

and optical properties. The biological profile of both NPs was evaluated by examining interactions with bacteria, proteins and DNA while bioaffinity, biocompatibility and toxicity of NPs were also estimated [22, 23, 24]. Antibacterial activity was investigated against the Gram-positive *B. subtilis*, *B. cereus* and *S. aureus* and the Gram-negative *E. coli* and *X. campestris*. DNA interactions/damage induced by NPs was estimated through treatment of plasmid pUC18 DNA (pDNA), and then separation of DNA interaction products on agarose gel electrophoresis. Possible cytogenetic and genotoxic effects of NPs were examined by the Sister Chromatid Exchange (SCE) assay, a simple, rapid, very sensitive and well-established method for evaluating human exposure to different chemical and mutagenic agents, while also being a toxicity assessment for detecting chromosome instability or DNA damage. NP's genotoxicity was estimated based on a) the frequency of SCEs, b) cytostaticity on the Proliferating Rate Indices (PRIs) and c) cytotoxicity on the Mitotic Indices (MIs). Irinotecan (CPT) was utilized as standard genotoxic agent. The NP's *In vitro* anti-inflammatory capacity was measured using the albumin denaturation assay while acetylsalicylic acid (aspirin) was used as a standard reference drug. The bioreactivity of NPs was evaluated in comparison with one another to further investigate copper-iron synergistic phenomena. Ultimately, the subject of NPs' behavior on bio-applications stands as a concentration dependent issue where the goal is to effectively trigger the desired effect (e.g. inhibit microorganisms and/or inflammation) in an applied dose where no undesired toxicity is observed.

2. Results and Discussion

2.1. Synthetic aspects and structural characterization

$CuFeO_2$ mainly adapts the R3m rhombohedral crystal structure where FeO_6 octahedra that share the [FeO_2] edge form a layer and Cu^{+1} linearly bond to two O^{-2} ions form a second layer [25]. Till now, $CuFeO_2$ crystals have been prepared through high temperature syntheses, either solid-state, sol-gel or hydrothermal approaches, and mostly in the microscale [25, 26, 27, 28, 29]. Wet chemical hydrothermal approaches are based on bottom up formation of NPs through specific synthetic mechanisms, like the transformation of ions into their hydroxides followed by dehydration/reduction at higher temperatures [30] and provide more precision in the isolation of desired products. Additionally, such attempts in a relative lower temperature (<200°C) can effectively lead to nanocrystals by avoiding extended growth and aggregation of particles that take place in higher temperature [31, 32, 33, 34, 35, 36]. Still no lucid formation mechanism for $CuFeO_2$ nanocrystals is given and reproducible synthesis of $CuFeO_2$ NPs is challenging.

In the current work, we employed a combined reduction/hydrothermal synthetic route to successfully obtain pure $CuFeO_2$ nanoparticles at 150ºC. Hydrazine, $N_2H_4.H_2O$, was utilized in a double role of reducing agent and pH adjuster. Given the fact that hydrazine has basic (alkali) properties similar to ammonia (K_b = 1.3 x 10^{-6}, K_b = 1.78 x 10^{-5} for hydrazine and ammonia, respectively), an excess was used to adjust the pH of the solution. Furthermore, hydrazine is a weak reducing agent that does not affect the oxidation state of $Fe^{3+}_{(aq)}$ but is able to reduce $Cu^{2+}_{(aq)}$ to $Cu^{1+}_{(aq)}$, that is required for the desired $Cu^{1+}Fe^{3+}O_2$ crystal structure. Additionally, following the same synthetic pathway and in the absence of iron precursor, Cu_2O nanoparticles were effectively synthesized. In both cases, a small amount of polyethylene glycol was added during the synthesis to enhance the hydrophilicity and colloidal stability of the as-produced nanoparticles.

Fig.1 illustrates the room temperature powder XRD diffractographs for $CuFeO_2$ (Fig.1A) and Cu_2O nanoparticles (Fig.1B). The Bragg reflection peaks for $CuFeO_2$ at 2θ of 15.40º, 31.19º, 34.46º, 35.65º, 40.15º, 43.24º, 47.58º, 55.16º, 60.99º, 64.75º 70.15º, 72.79º, 75.73º, 86.80º and 87.83º correspond to the reflections from the (0.0.3), (0.0.6), (1.0.1), (0.1.2), (1.0.4), (0.1.5), (0.0.9), (0.1.8), (1.1.0), (1.0.10), (0.1.11), (2.0.2), (0.2.4), (2.0.8), and (0.1.14) crystallographic planes of R3m rhombohedral $CuFeO_2$ nanoparticles (JCPDS no. 75-2146), respectively. Applying the Scherrer equation, based on the full width at half-maximum (FWHM) of all peaks, provided an average crystallite size of 32.4 nm, while lattice parameters were calculated by the means of MDI's Jade software at a = b = 3.0362Å and c = 17.2227Å and

are very close to the theoretical values (a = b = 3.035Å and c = 17.166Å). No peaks of common impurities such as CuO, Cu_2O, Fe_2O_3 and $CuFe_2O_4$ appear in the diffractograph, verifying the purity of the nanoparticles. For Cu_2O, peaks at 2θ of 29.58°, 36.39°, 42.20°, 61.25°, 73.44° and 77.57° correlate to the (1.1.0), (1.1.1), (2.0.0), (2.2.0), (3.1.1) and (2.2.2) crystallographic planes of Pn-3m cubic Cu_2O nanoparticles (JCPDS no. 65-3288), respectively, with an average crystallite size of 19.6 nm and lattice parameter a = b = c = 4.2767Å, very close to theoretical value of 4.26Å. Again, not any common impurities like CuO, Cu or $Cu(OH)_2$ are present in the sample.

The crucial role of hydrazine and autoclave use were certified by additional synthetic regulations; synthesis of Cu_2O NPs at room temperature (T1), hydrothermal synthesis of Fe_2O_3 NPs in the presence of hydrazine (T2) and synthesis of $CuFeO_2$ NPs in the absence of hydrazine (T3). These regulations were essential to elucidate the formation mechanism of $CuFeO_2$ NPs. Powder XRD diffractographs of the synthetic regulations are shown in Fig.2 (A to C, respectively). In case of T1 (Fig.2A) a mixture of Cu_2O and $Cu(OH)_2H_2O$ (JCPDS no. 42-0746). For T2, (Fig.2B) the presence of a-Fe_2O_3 (JCPDS no. 33-0664) is dominant. Ferric hydroxides are easily produced followed by dehydration at higher temperatures to give hematite nanoparticles [37]. Meanwhile, in the case of T3 (Fig.2C) a mixture of a-Fe_2O_3 and copper oxalate, C_2CuO_4 (JCPDS no. 46-0856) was isolated, indicating that nano-hematite can be generated even in a non-alkaline environment, as well as that the lack of hydrazine leaves copper in its highest oxidation state, Cu^{2+}. Regarding the oxalate formation, it has recently been proposed by us and others, that polyols and their oxidized derivatives such as carboxylates and oxalates can form relative stable intermediate complexes with metals ions [9, 38]. These complexes decompose at elevated temperatures.

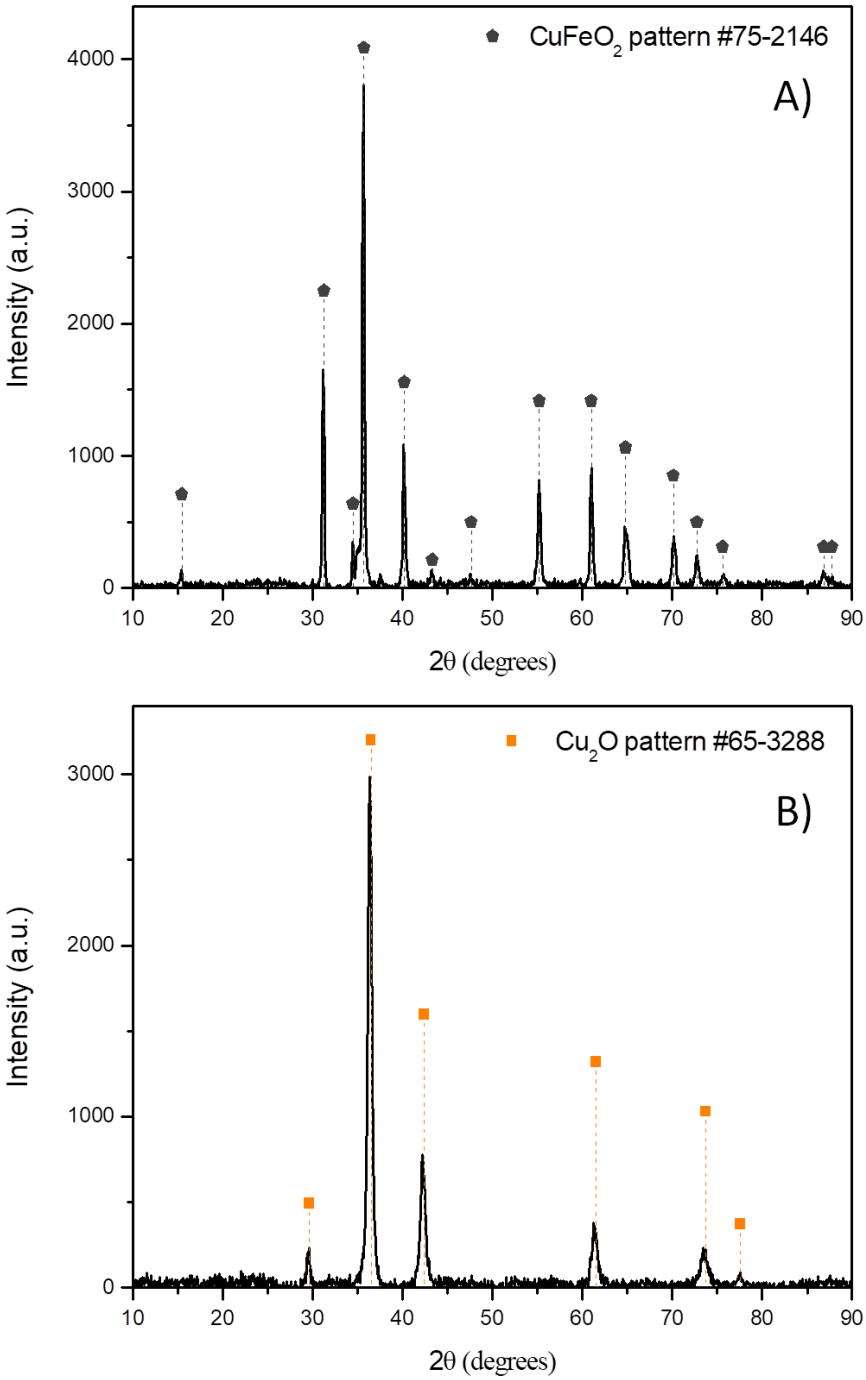

Figure 1. Powder X-ray diffraction (XRD) patterns of the synthesized $CuFeO_2$ (A) and Cu_2O (B) nanoparticles.

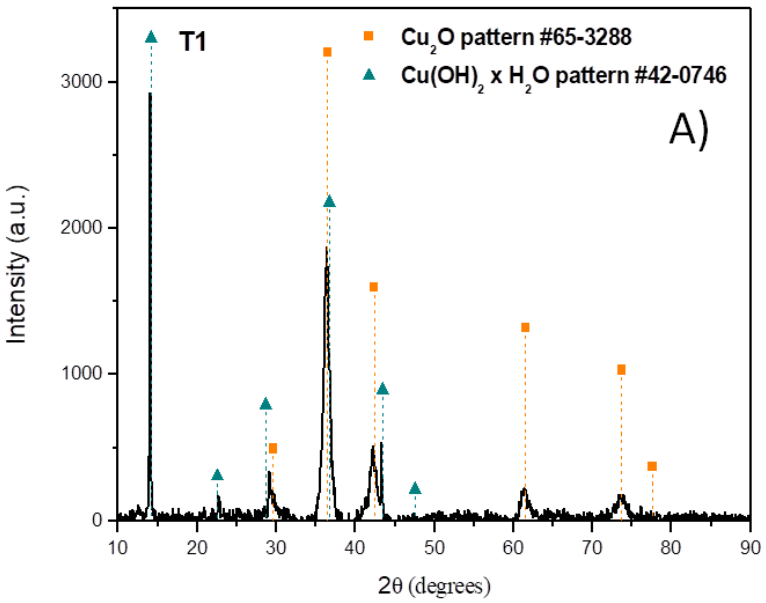
T1
Cu2O pattern #65-3288
Cu(OH)2 x H2O pattern #42-0746
A)
Intensity (a.u.)
2θ (degrees)

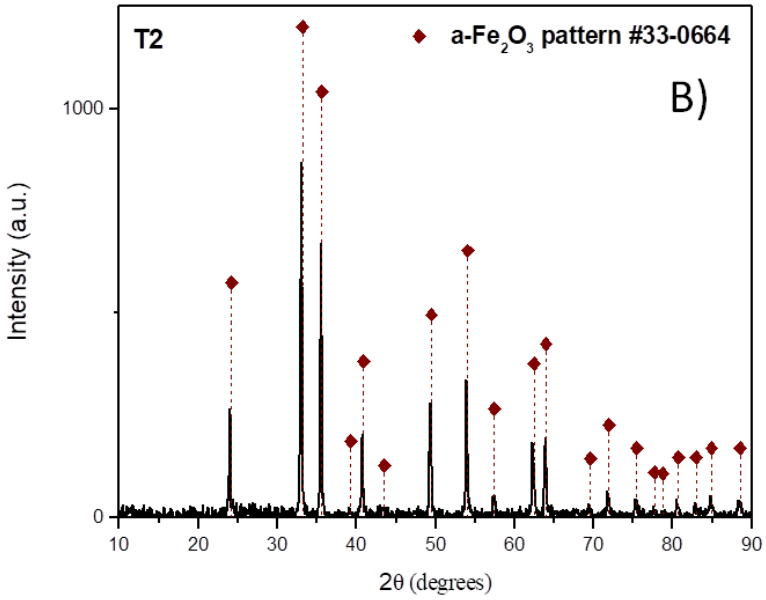
T2
a-Fe2O3 pattern #33-0664
B)
Intensity (a.u.)
2θ (degrees)

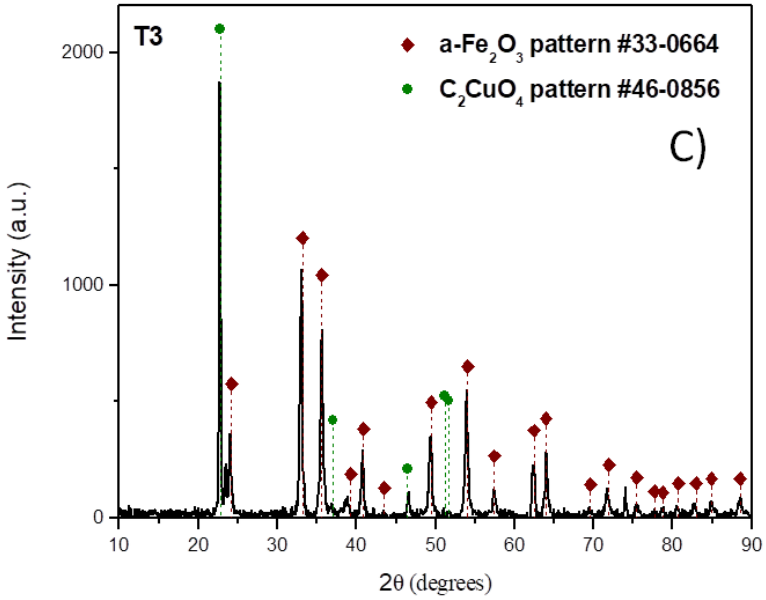
T3
a-Fe2O3 pattern #33-0664
C2CuO4 pattern #46-0856
C)
Intensity (a.u.)
2θ (degrees)

Figure 2. Powder X-ray diffraction (XRD) patterns for synthetic regulations T1-T3; synthesis of Cu_2O NPs at room temperature (A-T1), hydrothermal synthesis of Fe_2O_3 NPs in the presence of hydrazine (B-T2) and running the synthetic route for CuFeO2 NPs in the absence of hydrazine (C-T3).

Based on all the above, the formation mechanism of $CuFeO_2$ via the utilized combined reduction/hydrothermal synthesis is summarized by equations 1-6. At first, with the addition of hydrazine in the aquatic solution of copper and iron nitrate, Cu^{2+} and Fe^{3+} are transformed into $Cu(OH)_2xH_2O$ and $Fe(OH)_3$/FeOOH/$[Fe(H_2O)_6]^{3+}$ according to equations 1 and 3-5, respectively. Following that, $Cu(OH)_2xH_2O$ get reduced to cuprous oxide, Cu_2O (equation 2). Then, the solution is transferred into the autoclave where hydrothermal dehydration reactions dominate and hematite, Fe_2O_3, is produced (equations 3-5). Finally, $CuFeO_2$ NPs are formed from the reaction of hematite and cuprous oxide (equation 6).

$$\mathbf{Cu^{2+}_{(aq)} + 2OH^- + H_2O \rightarrow Cu(OH)_2xH_2O \ (1)}$$

$$\mathbf{4Cu(OH)_2xH_2O + N_2H_4xH_2O \rightarrow 2Cu_2O + 11H_2O + N_2 \ (2)}$$

$$\mathbf{2Fe^{3+}_{(aq)} + 6OH^- \rightarrow 2Fe(OH)_3 \rightarrow Fe_2O_3 + 3H_2O \ (3)}$$

$$\mathbf{2Fe^{3+}_{(aq)} + 6OH^- \rightarrow 2FeOOH + 2H_2O \rightarrow Fe_2O_3 + 3H_2O \ (4)}$$

$$\mathbf{2Fe^{3+}_{(aq)} + 12H_2O \rightarrow 2[Fe(H_2O)_6]^{3+} \rightarrow Fe_2O_3 + 9H_2O + 6H^+ \ (5)}$$

$$\mathbf{Cu_2O + Fe_2O_3 \rightarrow 2CuFeO_2 \ (6)}$$

It is important to mention that the utilization of an autoclave provides reproducibility and stability for the isolated NPs.

Raman, FTIR and UV-Vis spectroscopies were employed for additional identification of the structure of the samples. Fig. 3 represents the Raman spectra of $CuFeO_2$ NPs and the mixture of a-Fe_2O_3 and copper oxalate, C_2CuO_4 (synthetic regulation T3) along with photographs of the illuminated area provided by the optical microscope of the Raman laser apparatus. Raman scattering of delafossite type oxides ($CuFeO_2$), exhibiting point group C_{3v} and space group R3m, gives rise to 12 optical phonon modes, out of which two phonons with A_{1g} and E_g symmetry are Raman-active [26]. For $CuFeO_2$, peaks at 350 and 690cm^{-1} (Fig.3) match the modes A_{1g} and E_g, respectively, attributed to the vibration of Cu–O bonds along the

c-axis and the a-axis, with no other peaks in the spectrum. Furthermore, the mixture of copper oxalate and nano-hematite is also apparent according to reported Raman shifts in the literature [39, 40]. Raman spectrum of Cu_2O (Fig.S1) is in agreement with the expected shifts for Cu_2O as shown before by us [20]; the longitudinal optical phonon modes (LO) Γ_{12}^{-} & $\Gamma_{15}^{-(1)}$, the second-order overtone $2\,\Gamma_{12}^{-}$ and the red-allowed transverse phonon mode (TO) $\Gamma_{15}^{-(2)}$, with observed peaks at 100, 145, 217 and 625cm^{-1}, respectively.

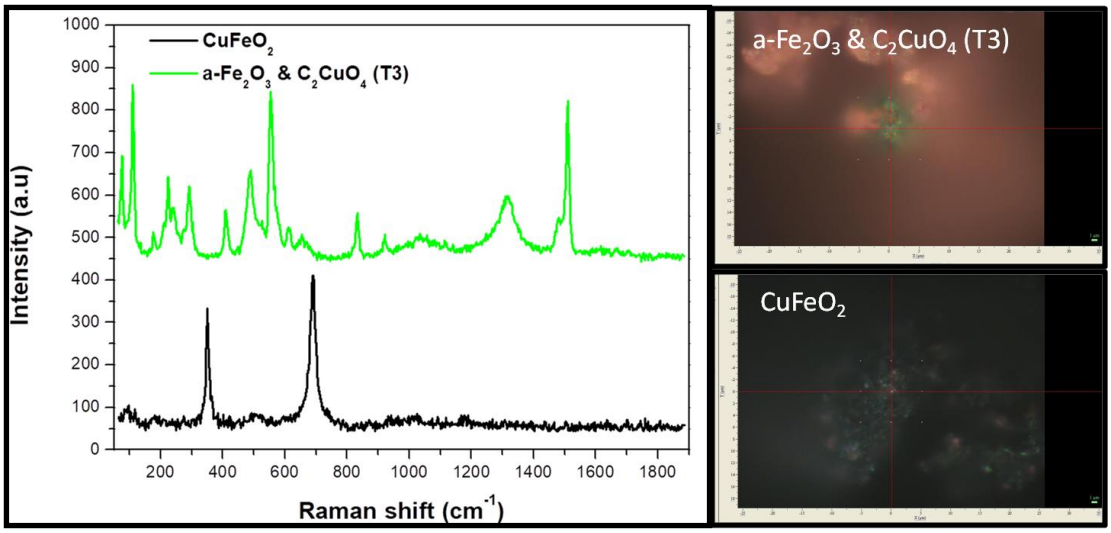

Figure 3. Raman spectra of $CuFeO_2$ NPs and the mixture of a-Fe_2O_3 and copper oxalate, C_2CuO_4 (synthetic regulation T3) along with optical microscope photographs of the illuminated area.

FTIR spectra of $CuFeO_2$ and Cu_2O (Fig.S2) reveal the characteristic M-O vibrations for both oxides. For $CuFeO_2$ NPs peaks at 420 and 665 cm^{-1} attributed to Fe(III)-O, Cu(I)-O vibrations respectively [35] while in case of Cu_2O NPs, Cu(I)-O vibration slightly shifted at 630 cm^{-1} [20]. Fig.S3 displays the UV-Vis spectra of aquatic suspensions of $CuFeO_2$ and Cu_2O shown λ_{max} at 815cm^{-1} and 580cm^{-1} for $CuFeO_2$ and Cu_2O, respectively. Experimental bang gaps were calculated via Tauc plots at 1.52 and 2.13eV and are close to the theoretical values 1.33 and 2,17eV, for $CuFeO_2$ and Cu_2O, respectively [41, 42]. The slight shift from the theoretical value in the calculated bang gap for $CuFeO_2$ is attributed to the nanoscale effect.

Particle size and morphology were examined through transition elector microscopy (TEM). Bright field images of $CuFeO_2$ and Cu_2O are portrayed in Fig.4 (A and B, respectively). $CuFeO_2$ NPs adapt the crystalline rhombohedral morphology [30, 34] with well-defined edges and corners for particles of 150-220nm while found more truncated, anisotropic, with defects and pseudo-hexagonal for particles of 90-150nm. Numberweighted size derived from counting over 40 $CuFeO_2$ NPs (fitted with a standard log-normal function) was measured at 123 ± 9.5

nm and it stands as one of the smallest sizes currently reported for $CuFeO_2$ crystals. TEM image of Cu_2O NPs (Fig.4B) illustrates cubic shaped and much smaller NPs with a measured average size of 24.5 ± 0.6nm.

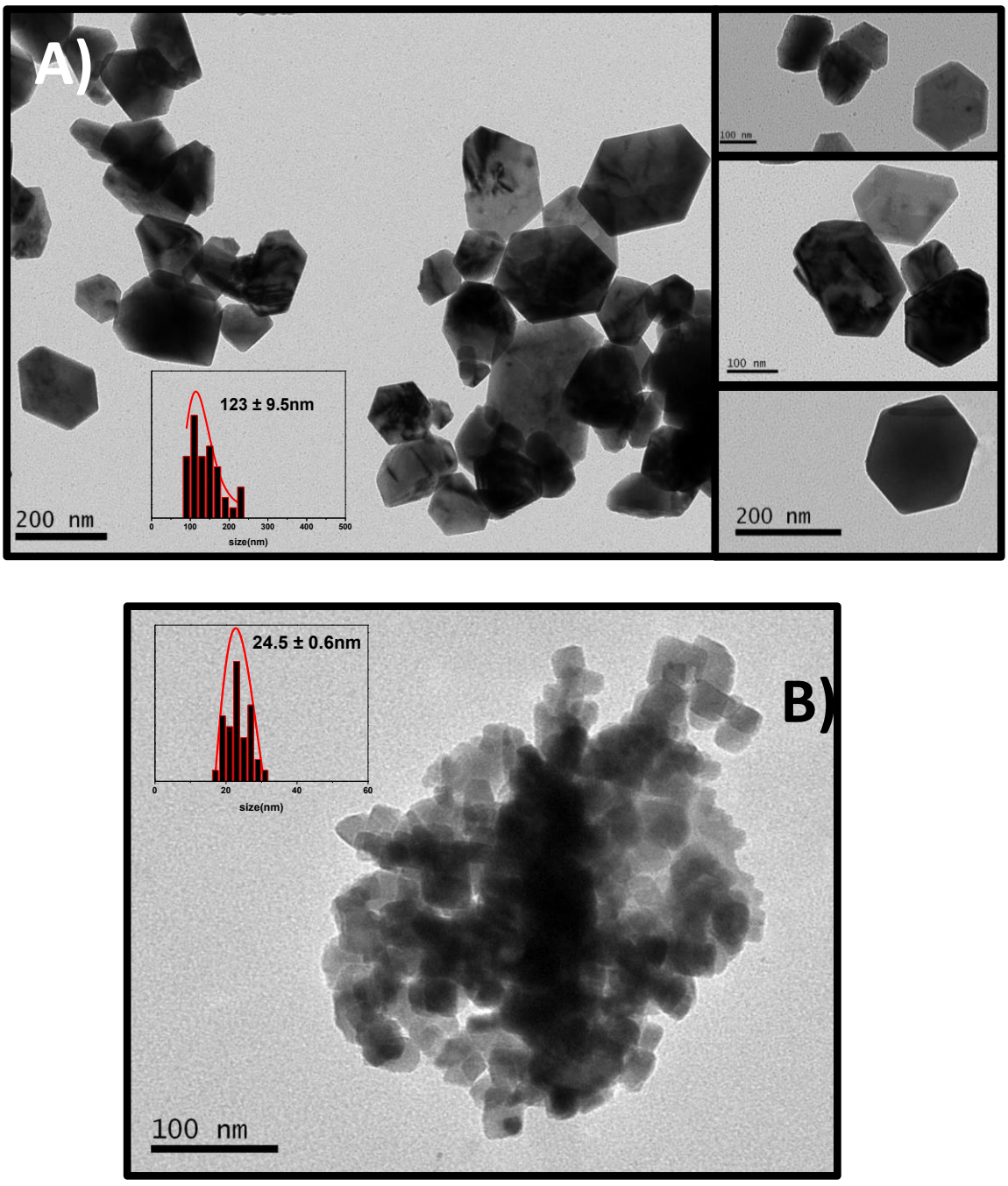

Figure 4. Transmission electron microscopy (TEM) images of the synthesized $CuFeO_2$ (A) and Cu_2O (B) nanoparticles along with their size distribution profiles derived from measuring over 40 NPs in each case.

2.2. Biological activity evaluation of $CuFeO_2$ and Cu_2O NPs

2.2.1. Evaluation of bacterial inhibition and antibacterial activity of NPs

Five bacterial strains have been utilized, the Gram-positive *B. subtilis*, *B. cereus* and *S. aureus* and the Gram-negative *E. coli* and *X. campestris*. The antibacterial activity of $CuFeO_2$ and Cu_2O NPs was estimated in terms of growth inhibition by measuring the optical density of bacterial cultures at 600 nm, 24 h after the injection of various suspensions of NPs (ranging from 2.5 to 100 μg/mL) into the cultures. In parallel, controls were also included in the experiment as cultures grown without NPs and negative control cultures (without bacterial cells) grown in the presence of pure NPs. Bacterial growth in the absence of NPs represents the 100% optical density value. Results are given in Fig.5 and given values are the averages of three measurements. Additionally, a nonlinear curve fit-growth/sigmoidal-dose response was applied to the data shown in Fig. 5 to calculate the Minimal Inhibitory Concentration (MIC) values (IC_{50}) linked to the 50% of the bacterial growth inhibition and summarized in Table 1. It is apparent from the data that $CuFeO_2$ NPs exhibited only a mild antibacterial activity, either by reaching a growth inhibition plateau in concentrations above 12.5 μg/ml (*E coli, B. cereus* and *S. aureus*) or by following a steady concentration-dependent manner in their inhibition (*X. campestris* and *B. subtilis*) but only up to 40% inhibition for the highest concentration tested (100 μg/ml). In so, all calculated IC_{50} values for $CuFeO_2$ NPs are >100 μg/ml. In contrast, Cu_2O NPs displayed a much stronger antibacterial activity, following a concentration-dependent manner in the inhibition of all tested bacterial strains with IC_{50} values all <12.5 μg/ml expect for *E. coli* (23.2 ± 0.63 μg/ml). More specifically, an antibacterial efficiency order may be given as follows: *B. cereus (*6.9 ± 0.51), *X. campestris* (7.2 ± 0.53), *B. subtilis* (9.1 ± 0.56), *S. aureus* (10.5 ± 0.61) and *E. coli* (23.2 ± 0.63). These results also showed that NPs did not exhibit a stronger antibacterial efficacy in respect to the type of Gram-negative or Gram-positive bacteria but rather in respect of the strain [69]. The cause of the different antibacterial behavior of the NPs may lie in the structural and compositional differences of bacterial cells' membrane. It is known that peptidoglycan cell membranes are thicker, thus preventing the NPs to penetrate them easily and in turn result in a lower antibacterial response. *E.coli* seems to be the most resistant because it possesses a special cell membrane structure with an important ability to resist antimicrobial agents.

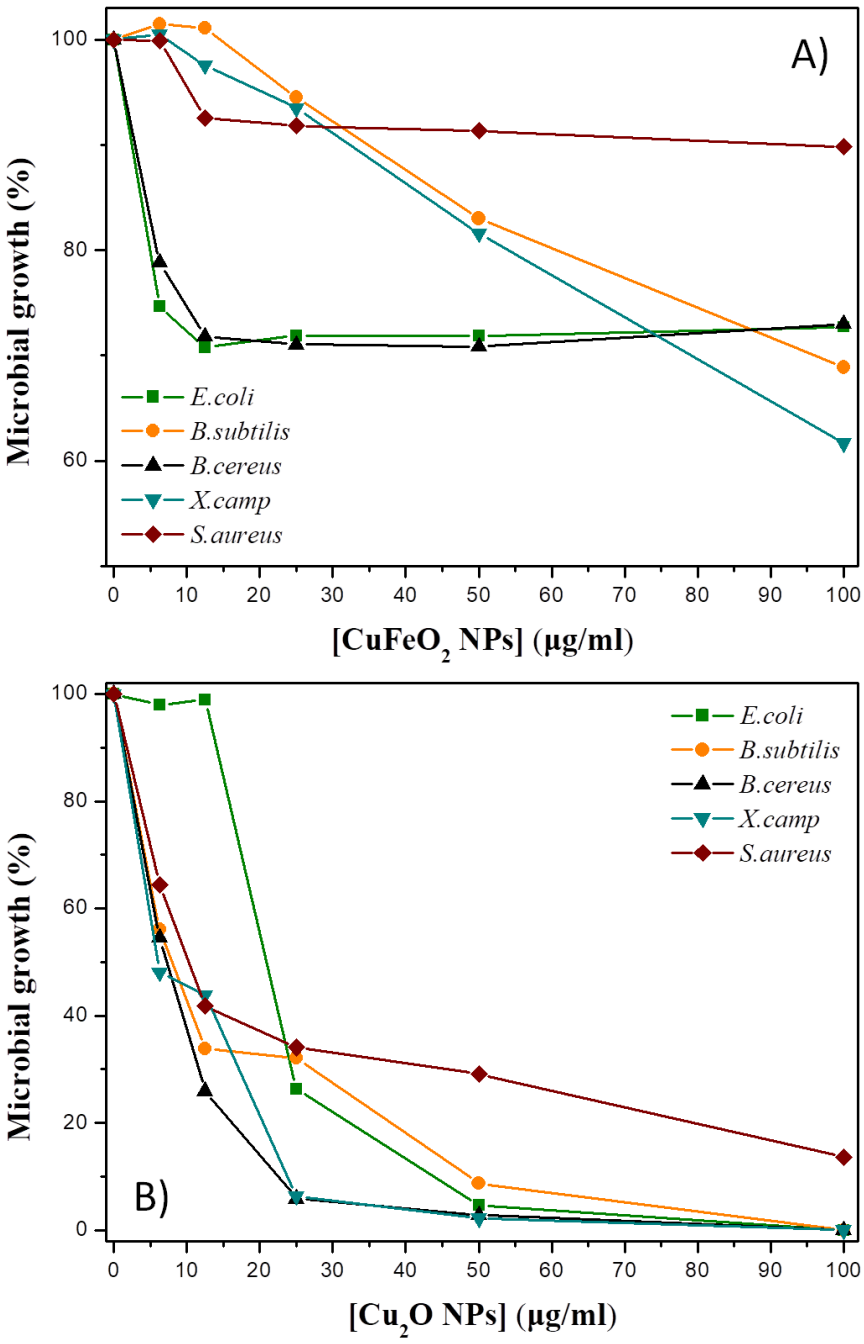

Figure 5. Bacterial growth inhibition curves (%) constructed via optical density measurements at 600 nm (OD_{600}) after the incubation of 5 different bacterial cultures (*E. coli*, *B. subtilis*, *B. cereus*, *X. campestris*, *S. aureus*) with A) $CuFeO_2$ and B) Cu_2O NPs. Values are mean of three replicates.

Regarding the comparison between Cu_2O and $CuFeO_2$ NPs, it looks that combining copper(I) and iron(III) in hetero oxide nanoparticle does not improve antibacterial efficiency compared to copper oxide nanoparticles, while the copper(0)-iron(0) biorelation was found fruitful in our previous work on the antimicrobial activity of CuFe bimetallic NPs [9]. This can

be attributed to the different oxidation states/redox dynamic of $CuFeO_2$, although it is important to mention that differences in crystallite and TEM size can also be the factors.

Table 1. Antibacterial activity of $CuFeO_2$ and Cu_2O NPs evaluated by the Half-Minimal Inhibitory Concentration (IC_{50}) values (μg/mL) provided by a nonlinear curve fit-growth/sigmoidal-dose response on the experimental optical density data. Values are mean of three replicates.

Bacterial strain	***E. coli***	***B. subtilis***	***B.cereus***	***X. campestris***	***S.aureus***
NPs	**IC_{50} (μg/mL)**				
$CuFeO_2$	>100	>100	>100	>100	>100
Cu_2O	23.2 ± 0.63	9.1 ± 0.56	6.9 ± 0.51	7.2 ± 0.53	10.5 ± 0.61

2.2.2. DNA binding/cleavage/damage experiments in agarose gel electrophoresis

Plasmid DNA (pDNA) can appear in one/ or some of five conformations, *Nicked open-circular, Relaxed circular, Linear, Supercoiled* and *Supercoiled denatured,* in the as given order of electrophoretic mobility from slowest to fastest, respectively. Given the presence of a break in only one of the strands of circular forms, the DNA will remain circular, but the break permits rotation around the phosphodiester backbone and the supercoils will be released. Therefore, for the same DNA, the supercoiled conformation runs faster than the circular forms. If the DNA sustains double stranded breaks it produces a linear conformation. Linear DNA runs through a gel end first and thus generate less friction than open-circular DNA, but more than supercoiled, and will migrate at a rate intermediate between the two. One of the crucial enzymes involved in the monitoring of the topological supercoiled state of DNA during cellular processes such as DNA replication, transcription, and recombination are topoisomerases [43, 44]. Topoisomerases cause scissions on the supercoiled form of the pDNA and thereby transform it to a lesser degree supercoiled form or to a linear, relaxed and/or nicked open-circular form. This happens through a temporary DNA breakage by a disruption of a phosphodiester bond, and by the concomitant creation of a covalent bond between the tyrosyl-residue of the enzyme with the 3′ end of disrupted DNA phosphodiester bond. Once the DNA has relaxed, topoisomerases re-ligate the cleaved DNA.

The interaction of NPs, $CuFeO_2$ and Cu_2O with pDNA (cleavage/damaging reactions) was monitored after their incubation with plasmid pUC18 DNA and separation of the obtained products using agarose gel electrophoresis. Photographs of the NPs-pDNA interaction are shown in Fig. 6. pDNA in the absence of NPs (control lane) appear in both the relaxed and the supercoiled form in a ≅ 50/50% state.

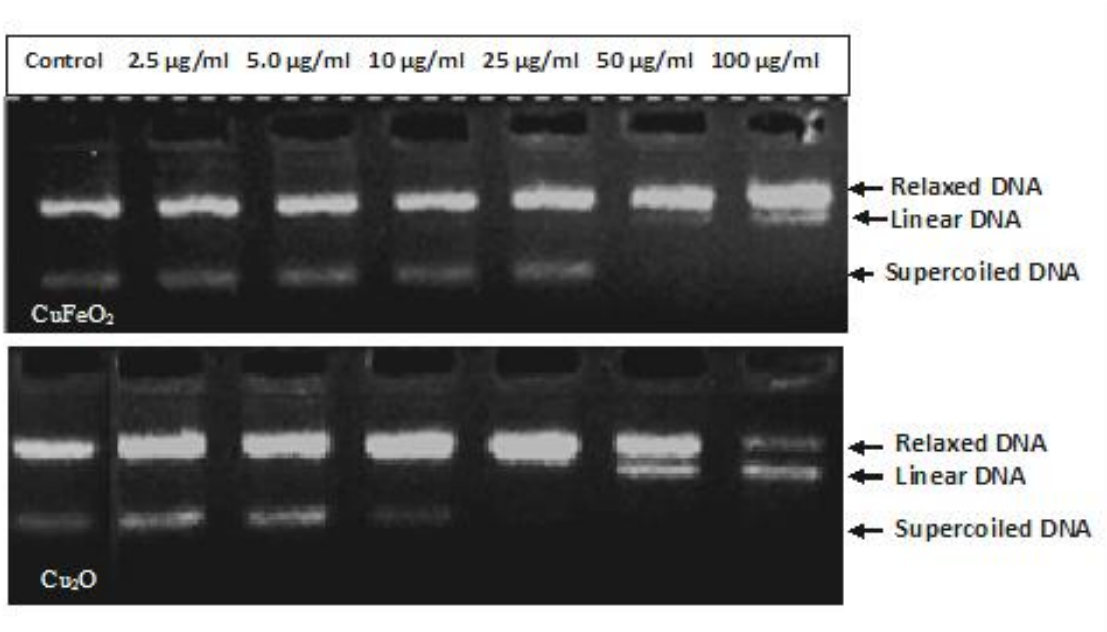

Figure 6. Agarose gel (1% w/v) electrophoretic pattern of an EthBr stained mixture of supercoiled and relaxed DNA, pDNA (pUC18) after a 2 h duration of electrophoresis. Each well contains 3 µg of pDNA mixed with various concentrations [0 (control), 2.5, 5, 10, 25, 50, and 100 µg/ml] of $CuFeO_2$ (up) and Cu_2O (down) NPs, incubated at 37 ^oC for 1 h.

Specifically, the pDNA cleavage efficiency of NPs was estimated by determining their ability to convert the supercoiled form (SC) to the relaxed circular form (R), the nicked circular form (NC) and/or the linear (L) form of pDNA. NPs' cleavage efficiency translates to mimicking topoisomerases' activity. The supercoiled DNA generally is first transformed in relaxed (by DNA single-stranded cleavage of one phosphodiester bond) and the supercoiled and relaxed may be then transformed in linear (by DNA double-stranded cleavage of two phosphodiester bonds) of the plasmid DNA. DNA damage induced by NPs is considered as toxicity on the genetic material (genotoxicity).

When pDNA was incubated with low concentrations of both NPs (up to 5 µg/ml), no change is observed as estimated by the photograph (Fig. 6). Moving further to the 10 µg/ml dose, the cleavage/ topoisomerases' activity mimicking began for Cu_2O with the decrease in the supercoiled zone. The sc DNA band gradually diminished until its disappearance, which

occurred in the 50 and 100 μg/ml concentrations for $CuFeO_2$ NPs, whereas this phenomenon started from the 25 μg/ml dose for Cu_2O NPs, suggesting a stronger interaction with DNA for Cu_2O NPs. Moreover, formation of the linear form of the pDNA was observed (Fig. 6), which migrated between supercoiled and relaxed circular bands for the 50 and 100 μg/ml concentrations of both NPs. These results revealed that both type of NPs mimic the mode of action of topoisomerases, as the same electrophoretic pattern is remarked for topoisomerase I [45]. However, toxicity in the form of DNA damage was unveiled for Cu_2O NPs for the 100 μg/ml dose as a significant decrease in relaxed and linear forms was recorded, while no such observation was collected for $CuFeO_2$ NPs.

2.2.3. Sister Chromatid Exchange (SCE) assay

Many chemical agents such as NPs are possible DNA damaging mediators and while some of them might be used as potential antimicrobial and/or anticancer agents it remains an issue of selectivity on microorganisms and/or cancer cells against normal cells. Following the toxicity evaluation on pDNA and CT-DNA, the toxicity of $CuFeO_2$ and Cu_2O NPs was investigated on human cellular DNA by the sister chromatid exchange (SCE) assay. The Sister Chromatid Exchange (SCE) assay is a simple, rapid, very sensitive and well-established cytogenetic and genotoxic method for evaluating human exposure to different chemical and mutagenic agents, while also being a toxicity assessment for detecting chromosome instability or DNA damage [46, 47, 48, 49, 50]. Induction of SCEs is an essential tool of genotoxicity in *in vitro* [51] and *in vivo* studies [62, 64] as SCEs' methodology is more sensitive than many other cytogenetic methods, like chromosome abnormalities or micronucleus test. The failure of repair mechanisms to achieve recovery leads to DNA damage and strand breaks, resulting in an increase of SCEs frequencies [52, 53].

Recently, studies on NPs revealed biological effects such as DNA damage and cell kinetic parameters. Investigating increasing nanoparticle concentrations and different nanoparticle sizes has shown that NPs caused significant enhancement on sister chromatid exchange, micronuclei and chromosome aberration as compared to untreated cultures. The obtained *in vitro* results revealed that NPs had dose-dependent effects on inducing oxidative damage, genotoxicity and cytotoxicity in human blood cells [46, 49].

In this study $CuFeO_2$ and Cu_2O NPs have been found to produce genotoxic, cytotoxic and cytostatic action. Results derived from 4 different concentrations (6.2, 10, 25 and 50 μg/ml) are summarized in Table 2 where camptothecin-11 (CPT) values are also included as reference. Results are based on chromosome captions of the SCE assay (captions of different metaphases

are given in Fig.7) and SCEs were evaluated in the 2nd division metaphase where one chromatid of each chromosome is dark stained (Fig.7B).

Table 2. *In vitro* genotoxic and cytogenetic effects of NPs in normal peripheral lymphocytes. Evaluation of SCEs was based on 30-40 second division cells and results were based on two experiments with the same protocol. At least 200 metaphases were measured for the estimation of PRIs and 2000 lymphocyte nuclei were scored for the MIs. Where CPT = Irinotecan (Camptothecin-11), SEM= Standard Error of the Mean and EV= Expected Value (EV_{Cu2O} = [OV_{Cu2O-} $OV_{Control}$] + OV_{CPT}). [a] $p < 0.01$ vs. all lines, [b] $p < 0.01$ vs. control, [c] $p < 0.01$ vs. all NPs, [d] $p < 0.01$ vs. all previous lines, [e] $p < 0.01$ vs. respective $CuFeO_2$, [f] $p < 0.05$ vs. control and all $CuFeO_2$, [g] $p < 0.05$ vs. all lines, [h] $p < 0.05$ vs. control, [i] $p < 0.05$ vs. line 2, [j] $p < 0.05$ vs. line 9, [k] $p < 0.05$ vs. line 10, [l] $p < 0.05$ vs. line 18.

No	NPs	Concentrations of NPs (µg/ml)	Mean SCEs/cell ± SEM (range)	PRI	MI (‰)
1	**Control**	-	6.43 ± 0.26[a] (4–9)	2.14	22.5
2	**$CuFeO_2$**	50	21.64± 1.45[b] (13–24)	1.55[f]	15.5[h]
3	**$CuFeO_2$**	25	19.77± 1.34[b] (17–28)	2.01	23.5[i]
4	**$CuFeO_2$**	12.5	15.60± 1.02[b] (12–23)	2.13	25.5[i]
5	**$CuFeO_2$**	6.2	13.00± 0.99[b] (8–22)	2.28	33.0[h,i]
6	**Cu_2O**	50	-	-	0.0[h,e]
7	**Cu_2O**	25	30.18 ± 3.49[b,c] (19–47)	1.27[f,g]	1.0 [h,e,j]
8	**Cu_2O**	12.5	16.75 ± 1.57[b] (12–23)	1.39[f]	5.5 [h,e,j]
9	**Cu_2O**	6.2	16.00 ± 1.21[b] (12–19)	1.49[f]	8.0 [h,e]
10	**CPT**	-	44.72± 5.12[b,c] (22–63)	2.35	25.5
11	**$CuFeO_2$ + CPT**	50	57.72± 6.35[b,d] (42–69)	1.67[f]	22.5
12	**$CuFeO_2$ + CPT**	25	48.14± 5.91[b,e] (34–64)	1.83	23.5
13	**$CuFeO_2$ + CPT**	12.5	43.32± 4.82[b,e] (21–62)	2.11	32.5 [h]
14	**$CuFeO_2$ + CPT**	6.2	42.97± 4.40[b,e] (20–61)	2.15	35.5[h]
15	**Cu_2O + CPT**	50	-	-	0.0 [h,e,k,l]
16	**Cu_2O + CPT**	25	-	1.00[g]	2.0 [h,e,k,l]
17	**Cu_2O + CPT**	12.5	120.99± 10.62[a,d] (95–136) EV=55.04	1.44[g]	6.5 [h,e,k,l]
	Cu_2O + CPT	6.2	72.59± 9.08[a]	1.76	25.0

18			(54–101) EV=54.29		

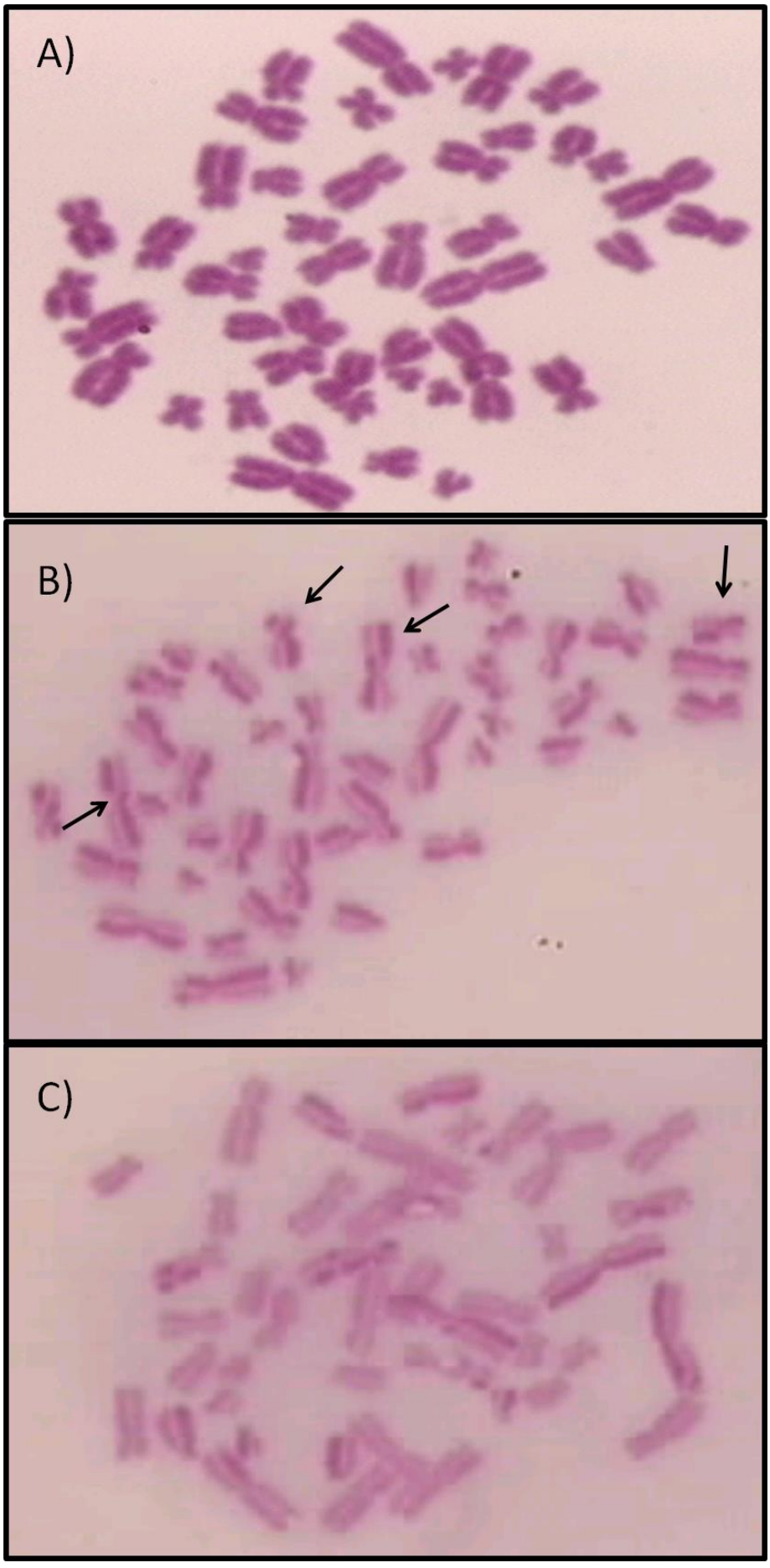
A)
B)
C)

Fig.7 Chromosome captions of the SCE assay where A) all chromosomes have both chromatids dark stained (1st division metaphase), B) one chromatid of each chromosome is dark stained (2nd division metaphase, SCEs can be evaluated only in these metaphases, arrows show SCEs), C) metaphase where a proportion of chromosomes have both chromatids light stained (3rd+ or subsequent division metaphase).

Addition of NPs, at all concentrations tested alone, induced statistically significant ($p < 0.01$) increases in SCEs frequencies comparing to control, while statistically significant ($p < 0.05$) reduction of PRIs and MIs were measured at higher concentrations of NPs (25 and 50μg/ml). However, it is evident from these results that $CuFeO_2$ displayed significantly decreased SCEs and increased PRIs and MIs compared to Cu_2O NPs. Additionally, the later NPs induced total chromosomal destruction in the 50 μg/ml dose and a similar form of toxicity was also observed in their interaction with pDNA at 100 μg/ml. Based on these results it appears that $CuFeO_2$ NPs display enhanced biocompatibility and less toxicity compared to Cu_2O NPs.

It has been proposed that successful DNA repair, prior to S phase, removes damage which otherwise might give rise to SCEs [54]. In normal human lymphocytes interference by NPs with DNA repair of CPT-induced DNA damage would lead to an increase in the number of incompletely repaired lesions, at the time the cells reach S phase in vitro, lesions which may subsequently give rise to SCEs and cell division delays (Table 3). While NPs showed increase of SCEs 2-6 times alone, the increase was 7-20 times in combination with CPT over the control value. Addition of CPT in these lymphocyte cultures also increased the frequencies of SCEs alone, but much more in combination with NPs, confirming its synergistic genotoxic and cytotoxic action in cultured human lymphocytes. The SCE induction, the MIs and the PRIs reduction were consistently much higher than those expected by the simple addition of the effects on SCEs, PRIS and MIs of the NP and CPT alone. Also, a correlation between PRI and MI was revealed ($p<0.05$ and $r= 0.907$) showing that cytotoxicity of NPs, with CPT or not, goes along with cytotoxicity in these cultures. Our present findings, concerning the combined treatment of NPs plus CPT, showed a high correlation between the potency for SCE induction, effectiveness in cell division delay and cytotoxicity. This is of considerable interest to the problem of cancer, because it provides a mechanism by which the rate of potential genetic damage, induced by potential chemotherapeutics, may be modified [55]. Cancer cells, like normal human cells, are capable in DNA repair mechanisms. Therefore, unrepaired DNA damage, expressed as SCEs, in normal cells by certain agents may indicate unrepaired DNA damage in cancer cells by the same chemicals. These may possibly indicate that the above combination may have a potential chemotherapeutic value.

2.2.4. Anti-inflammatory activity evaluation/albumin denaturation experiments

Protein denaturation is usual process during which the secondary and tertiary structures of proteins are destroyed resulting in loss of their biological function. Protein denaturation may be caused by a spectrum of reasons including heat, electrolytes, or alcohols which generate well-studied alterations in the solubility of albumins and globulins [56]. Protein denaturation can correlate with an inflammatory response and an inhibition in the denaturation after the addition of a chemical compound can be considered as an anti-inflammatory activity. NPs that can inhibit denaturation display a bioaffinity in albumin as well as considered anti-inflammatory candidates [57, 58, 59]. Herein, protein denaturation was triggered by heating of bovine serum albumin (BSA). Heating of BSA reflects in its denaturation and in antigens expression, that both are related with type-III hypersensitivity reaction, which in turn is associated to various diseases including rheumatoid arthritis, systemic lupus erythematosus, serum sickness, and glomerulonephritis [60]. Acetylsalicylic acid (aspirin) has shown a dose-dependent ability to inhibit thermally induced protein denaturation [66] and can be utilized as a reference along with that said chemical compound.

In this direction, albumin denaturation optical density measurements were used as an assay to calculate the anti-inflammatory capacity of $CuFeO_2$ and Cu_2O NPs. As $CuFeO_2$ NPs displayed significantly less toxicity than Cu_2O NPs both on pDNA interactions and on SCE assay it would be interesting to evaluate a property reflecting a curative/protective action like anti-inflammatory capacity in contrast to a damaging action that is antibacterial activity. Results derived from 6 different concentrations (2.5, 5, 10, 25, 50, and 100μg/ml) are summarized in Table 4 where aspirin values are also included as reference. Denaturation of albumin in the presence of distilled water is considered as 100% denaturation and 0% anti-inflammatory activity (Table 4). Both NPs followed a concentration dependent anti-inflammatory activity. Values for Cu_2O NPs are very close to the values obtained for aspirin and this phenomenon is already reported for other NPs in the literature [57, 58, 59], but it is the first report for copper-based NPs. Moreover, $CuFeO_2$ NPs exhibited a stronger anti-inflammatory capacity than Cu_2O and similar to aspirin as reflected in the values of Table 4. The copper(I)-iron(III) synergy appears to boost albumin bioaffinity and protective ability against protein denaturation, enhancing the anti-inflammatory response of $CuFeO_2$ NPs.

Table 4. Anti-inflammatory activity of various concentrations [0 (control), 2.5, 5, 10, 25, 50, and 100 μg/ml] of $CuFeO_2$ and Cu_2O NPs, as well as Aspirin (reference drug), measured as inhibitory percentage (%) of albumin denaturation.

Concentration of NPs/Aspirin (µg/ml)	Albumin denaturation (%)			Denaturation protection / Anti-inflammatory activity (%)		
	$CuFeO_2$	Cu_2O	Aspirin	$CuFeO_2$	Cu_2O	Aspirin
0 (control)	100	100	100	0	0	0
2.5	72.1	80.3	85.1	27.9	19.7	14.9
5	57.4	79.9	84.6	42.6	20.1	15.4
10	40.9	79.2	78.1	59.1	20.8	21.9
25	36.4	73.3	58.4	63.6	26.7	41.6
50	34.9	53.9	45.1	65.1	46.1	54.9
100	31.9	49.2	36.6	68.1	50.8	63.4

3. Conclusions

Copper formulations, ionic and bulk, have been applied as antimicrobials for centuries and research on copper-based NPs aims to lower dose and higher efficiency novel materials, but concerns for risk assessment, biocompatibility and human health should be taken into account. Although the antibacterial activity of $CuFeO_2$ NPs was found relatively weaker than the already established antimicrobial candidate Cu_2O NPs, interactions with pDNA and the sister chromatid exchange (SCE) assay unveiled significantly enhanced toxicity for Cu_2O NPs and enhanced biocompatibility for $CuFeO_2$ NPs. Moreover, and in the case of a curative and repairing action such as anti-inflammatory activity, $CuFeO_2$ NPs were found more capable in protein denaturation protection, with anti-inflammatory capacity similar to aspirin. The meeting of iron and copper in an heterometal copper(I)-iron(III) nano-oxide lessens the bio-damage, antimicrobial hostility and toxicity while strengthening the biocompatibility, bio-repair and protection against inflammation. We have to underline that the specific oxidation states govern the behavior of $CuFeO_2$ NPs, given that copper-iron synergy in bimetallic CuFe NPs showed enhanced antimicrobial action [9].

Moreover, SCE findings on combined treatment of NPs plus CPT showed a synergistic high correlation between the potency for SCE induction, thus providing a mechanism by which the rate of genetic damage may be modified. This indicates that the combination of cuprous NPs and CPT may have a potential chemotherapeutic value and sets futures thoughts on expanding our research on cancer cells and anticancer agents.

Supporting Information

Additional data with FTIR and UV-Vis spectroscopies' data for Cu_2O and $CuFeO_2$ nanoparticles.

Conflict of interest

The authors declare that there are no conflicts of interest

Acknowledgment

This research did not receive any specific grant from funding agencies in the public, commercial, or not-for-profit sectors.

4. Materials and Methods

4.1. Synthesis and structural characterization of NPs

4.1.1. Preparation of nanoparticles

A low-temperature (150 °C) combined reduction/hydrothermal process was utilized for the synthesis of $CuFeO_2$ nanoparticles. $Fe(NO_3)_3 \cdot 9H_2O$ (0.5 mmol, 0.202 g), $Cu(NO_3)_2 \cdot 3H_2O$ (0.5 mmol, 0.121 g) and polyethylene glycol, PEG 8000 (0.1875 mmol, 1.5 g) were mixed and dissolved in 8 ml of deionized water. The resulting mixture was stirred thoroughly at room temperature to produce a homogenous yellowish solution. The concentrations of $Fe(NO_3)_3 \cdot 9H_2O$, $Cu(NO_3)_2 \cdot 3H_2O$ and PEG 8000 were calculated to be 6,25 x 10^{-2} M, 6,25 x 10^{-2} M and 2,344 x 10^{-2} M, respectively. Then an excess of hydrazine hydrate, $N_2H_4.H_2O$ (4.1 mmol, 0.207 g, $[N_2H_4.H_2O]$ = 0.5 M) was added dropwise to the solution under vigorous stirring, adjusting the pH of the solution at 10 before a color change to grey-brownish yellow. After 30 minutes of stirring, the resulting solution was transferred into a 23 mL Teflon-lined stainless-steel autoclave where hydrothermal crystallization was carried out under autogenous pressure at 150 °C for 8 h in an oven. Then the autoclave was cooled naturally to room temperature and after centrifugation at 5000 rpm, the supernatant liquids were discarded, and a black precipitate was obtained and washed with ethanol, at least three times, to remove the excess of ligands and the unreacted precursors.

Cu_2O NPs: $Cu(NO_3)_2 \cdot 3H_2O$ (0.5 mmol, 0.121 g), polyethylene glycol, PEG 8000 (0.1875 mmol, 1.5 g), 8 ml of deionized water, hydrazine hydrate, $N_2H_4.H_2O$ (4.1 mmol, 0.207 g, $[N_2H_4.H_2O]$ = 0.5 M)

Synthetic regulation T1: $Cu(NO_3)_2 \cdot 3H_2O$ (0.5 mmol, 0.121 g), polyethylene glycol, PEG 8000 (0.1875 mmol, 1.5 g), 8 ml of deionized water, hydrazine hydrate, $N_2H_4.H_2O$ (4.1 mmol, 0.207 g, $[N_2H_4.H_2O]$ = 0.5 M). No hydrothermal step, synthesis at room temperature.

Synthetic regulation T2: $Fe(NO_3)_3 \cdot 9H_2O$ (0.5 mmol, 0.202 g), polyethylene glycol, PEG 8000 (0.1875 mmol, 1.5 g), 8 ml of deionized water, hydrazine hydrate, $N_2H_4.H_2O$ (4.1 mmol, 0.207 g, $[N_2H_4.H_2O]$ = 0.5 M).

Synthetic regulation T3: $Fe(NO_3)_3 \cdot 9H_2O$ (0.5 mmol, 0.202 g), $Cu(NO_3)_2 \cdot 3H_2O$ (0.5 mmol, 0.121 g), polyethylene glycol, PEG 8000 (0.1875 mmol, 1.5 g), 8 ml of deionized water.

All the reagents were of analytical grade and were used without any further purification: Copper(II) nitrate trihydrate $Cu(NO_3)_2 \cdot 3H_2O$ (Merck, ≥99.5%, M = 241.60 g/mol), Iron(III) nitrate nonahydrate $Fe(NO_3)_3 \cdot 9H_2O$ (Merck, ≥99.5%, M = 404 g/mol), polyethylene glycol (PEG) 8000 (Alfa aesar), Hydrazine hydrate $N_2H_4.H_2O$ (Merck, about 100%, M = 50.06 g/mol)

4.1.2. Characterization

X-Ray powder diffraction graphs (XRD) were recorded at Bragg-Brentano (BB) geometry using a two-cycles Rigaku Ultima+ powder X-ray diffractometer with a Cu Ka radiation operating at 40 kV/30 mA.

Conventional Transmission Electron Microscopy (TEM) images were obtained with JEOL JEM 1010 microscope operating at 100 kV. For TEM observations we have used suspensions of the nanoparticles deposited onto carbon-coated copper grids.

The micro-Raman measurements were performed at room temperature using the 515 nm line of a diode pumped solid state laser (Cobolt) as the excitation source. The power was kept at 0.1 mW, and an x100μm focus was used. The spectra were recorded using a micro-Raman LabRAM HR (HORIBA) system equipped with a peltier-cooled charge coupled device (CCD) detector. Additionally, photographs of the illuminated were captured by the optical microscope of the Raman laser apparatus. Fourier transform infrared spectra (400-4000 cm^{-1}) were recorded using a Nicolet FT-IR 6700 spectrometer with samples prepared as KBr pellets. UV/Vis spectra were recorded with a Hitachi U-2001 double-beam UV/Vis spectrophotometer.

4.2. Biological activity evaluation of $CuFeO_2$ and Cu_2O NPs

4.2.1. Materials for biological tests

Culture media: Two different media were used: (i) the Luria–Brettani broth (LB) containing 1% (w/v) tryptone, 0.5% (w/v) NaCl and 0.5% (w/v) yeast extract and (ii) the minimal medium salts broth (MMS) containing 1.5% (w/v) glucose, 0.5% (w/v) NH_4Cl, 0.5% (w/v) K_2HPO4, 0.1% (w/v) NaCl, 0.01% (w/v) $MgSO_4.7H2O$ and 0.1% (w/v) yeast extract. The pH of the media was adjusted to 7.0.

DNA cleavage/damage experiments in agarose gel electrophoresis: Agarose was purchased from BRL. Tryptone and yeast extract were purchased from Oxoid (Unipath Ltd., Hampshire, UK). All other chemicals were obtained from Sigma.

Plasmid DNA, pDNA (pUC18), was isolated from *Escherichia coli* (Top 10) using GenEluteTM HP endotoxin-free plasmid maxi prep preparation (Sigma–Aldrich), according to the manufacturer's specifications. The intercalative dye ethidium bromide (EthBr) was purchased from Sigma. Experiments were carried out in 50 mM Tris–Cl pH 7.5 buffer solutions to control the acidity of the reaction systems.

Sister Chromatid Exchanges (SCE) assay: Human peripheral blood samples were obtained from two male and two female donors, who were healthy medical students, not taking any medication, non-smokers and non-consumers of alcohol. Informed consent was taken from all donors and this study was approved by the University Ethics Committee. Human peripheral lymphocyte cultures were set up by adding 11 drops of heparinized whole blood from each of the four normal subjects to 5 mL of chromosome medium 1A (RPMI 1640, Biochrom, Berlin).

Anti-inflammatory activity evaluation/albumin denaturation experiments: Bovine albumin was purchased from Sigma (1% aqueous solution, Sigma-Aldrich, Germany). Reference drug, acetylsalicylic acid (aspirin) was purchased from Sigma.

All plastics and glassware used in the biological experiments were autoclaved for 30 min at 120 ^{o}C and 130 kPa. Heat-resistant solutions were similarly treated, while heat-sensitive reagents were sterilized by filter.

Stock suspensions of the NPs were prepared at a final concentration of 1 mg/ml by dissolving/suspending the NPs in water via the assistance of sonication bath.

4.2.2. Evaluation of bacterial inhibition and antibacterial activity of NPs

The antibacterial efficiency of the NPs has been estimated by its ability to inhibit the growth of microorganisms in the cultivation medium Mueller–Hinton broth (Imuna). Five bacterial species were used as follows: *Escherichia coli* (XL1), *Staphylococcus aureus* (ATCC 29213), *Bacillus subtilis* (ATCC 6633), *Bacillus cereus* (ATCC 11778), and *Xanthomonas campestris* (ATCC 33013) and their growth was monitored in the absence and presence of the $CuFeO_2$ and Cu_2O NPs. Bacterial growth was performed in LB, while the screening for antibacterial activity was carried out by determining the minimal inhibitory concentration (MIC) of the NPs [20]. The MIC (in μg/ml) value for each culture, expressed as IC_{50}, and defined as the lowest concentration that inhibited the bacterial growth by 50%, was determined based on batch cultures containing varying concentrations of NPs. Specifically, using the method of progressive double dilution in MMS with final concentrations of NPs equal to 6.25, 12.5, 25, 50 and 100 μg/ml, the MIC values were determined. In details, the concentration of microorganisms in the cultivation medium was 10^5–10^6 cfu/ml after pre-cultures were cultivated in LB overnight at their optimal growth temperature to assure the sufficient bacterial growth. Then, aliquots of 2 ml of MMS were inoculated with 20 μL of a pre-culture of each bacterial strain (cultures of reference). A second group of the same cultures supplemented with the suitable concentration of the NPs was evaluated. A third group of cultures with the same concentration of the NPs but without bacterial pre-cultures and was used as cultures of reference to check the effect of each type of NPs on MMS. All measurements were in triplicate. The growth of bacteria was monitored by measuring the turbidity of all culture groups at Abs_{600} after 24 h, determined using a spectrophotometer (Thermo Electron Corporation, Helios γ, USA). Turbidity measurements in the cultures of references (absence of NPs) represent the 100% of Bacterial growth. A nonlinear curve fit-growth/sigmoidal-dose response was applied to estimate IC_{50} values. All pre-cultures and cultures were incubated at 37 ^{o}C, except *X. campestris* that was cultivated at 28 ^{o}C.

4.2.3. DNA cleavage/damage experiments in agarose gel electrophoresis

The DNA fragmentation phenomenon caused by $CuFeO_2$ and Cu_2O NPs was watched using agarose gel electrophoresis. The effect of the NPs was examined *in vitro* by treating the pDNA with NPs suspensions of gradually increasing concentrations ranging from 2.5 to 100 mg/ml. In particular, reactions which contained aliquots of 5 μg of pDNA, were incubated at a constant temperature of 37 ^oC for 60 min in the presence of each type of NPs in a buffer A that maintained pH at 7.5 to a final volume of reaction at 20 μl. Then, reactions were terminated by the addition of 5 μl loading buffer consisting of 0.25% bromophenol blue, 0.25% xylene cyanol FF (acid blue 147) and 30% glycerol in water. After incubation, the DNA products resulting from this interaction were separated by electrophoresis on agarose gels (1% w/v), which contained 1 μg/ml ethidium bromide in 40 x 10^{-3}M Tris–acetate (pH 7.5), 2 x 10^{-2}M sodium acetate, 2 x 10^{-3} M Na_2EDTA, at 5 V/cm. Agarose gel electrophoresis was performed in a horizontal gel apparatus (Mini-SubTM DNA Cell, BioRad) for about 2 h. The gels were visualized after staining with the fluorescence intercalated dye ethidium bromide under a UV illuminator which forms a fluorescent complex when it binds to DNA. The DNA cleavage/damage efficiency of NPs was estimated by determining the degree of electrophoretic mobility reflected in an up- or down-shift of the DNA to higher/or lower molecular weight DNA products respectively. Regarding pDNA, under electrophoretic conditions on an agarose gel, applied to circular plasmid DNA, the fastest migration will be noticed for DNA of closed circular forms (Form I, supercoiled). After a one strand cleavage, the supercoil will be relaxed to produce a slower-moving nicked form(Form II, relaxed), while after a double-stranded cleavage, a linear form of pDNA (Form III, linear) will be generated that migrates in between.

4.2.4. Sister Chromatid Exchange (SCE) assay

For SCEs evaluation, we add a) 5-bromodeoxyuridine (BrdU) at human peripheral lymphocyte cultures of 2 healthy individuals in a concentration of 5 mg/ml, b) $CuFeO_2$ and Cu_2O NPs and c) Irinotecan (CPT), added at a final concentration of 50 mg/ml, at the beginning of 72 h. CPT is a multi-used anticancer agent and a semisynthetic analogue of camptothecin-11 used in this study as a positive genotoxic agent, to induce a high frequency of SCEs and to reveal any underlying chromosomal instability [61, 62]. A total of 18 cultures were evaluated, a blank one (control), one supplemented only with CPT, four cultures with 6, 12.5, 24 and 50 μg/ml $CuFeO_2$ NPs, four cultures with 6, 12.5, 24 and 50 μg/ml of $CuFeO_2$ NPs + CPT, four cultures with 6, 12.5, 24 and 50 μg/ml of Cu_2O NPs and four cultures with 6, 12.5, 24 and 50 μg/ml of Cu_2O NPs + CPT. The above protocol has been executed twice. All cultures were kept in the dark to minimize photolysis of the BrdU and were incubated for 72 h at 37°C. Two hours before harvesting, colchicine was added at a final concentration of 0.3 mg/ml. Metaphases were collected and air-dried preparations were stained by the Fluorescence Plus Giemsa (FPG) technique [63] and scored for cells undergoing first mitosis (where both chromatids are dark

stained, Fig.7A), second (where one chromatid of each chromosome is dark stained, Fig.7B) and third and/or subsequent mitosis (where a proportion of chromosomes have both chromatids light stained, Fig.7C). Mean SCEs were measured only in suitable second division metaphases and at least 30-40 well spread and differentiated metaphases were blindly counted per culture, because, only at this stage, we were able to observe and count them. In order to establish PRI, at least 200 cells were counted and the following formula was used: PRI = $(M_1+2M_2+3M_{3+})/N$, were M_1 is the percentage of cells at first division, M_2 is the percentage of cells at second division and M_{3+} is the percentage of cells at third and subsequent divisions, while N is the total number of cells counted. Finally for the MIs, at least 2000 activated lymphocytes were determined for each culture [64]. Statistical analysis of the MI and PRI values was done by χ^2-test, while for the SCE frequencies the one-way analysis of variance (ANOVA) and subsequent the Duncan test were used to compare and evaluate different treatments and values. Furthermore, correlations between SCEs, PRIs and MIs were calculated by Pearson's correlation coefficient (r)[65].

4.2.5. Anti-inflammatory activity evaluation/albumin denaturation experiments

To evaluate the anti-inflammatory activity of $CuFeO_2$ and Cu_2O NPs, albumin denaturation in the presence of NPs was examined. In detail, NPs were mixed with 1% w/v aqueous solution of bovine albumin to reach final NPs' concentration of 6.25, 12.5, 25, 50 and 100 μg/ml. The mixtures were incubated at 37°C for 20 min, and subsequently heated at 51°C for 20 min to prop up the denaturation of albumin. The turbidity of the solutions was measured spectrophotometrically at 660 nm. Aspirin was used as the reference drug [66]. Denaturation of albumin in the presence of distilled water is considered as 100% denaturation. The protection of protein denaturation (%), hence the anti-inflammatory activity of NPs was calculated according to the following formula [67]:

$$\% \text{ Protection} = 100 - \left(\frac{OD\ of\ sample\ tested}{OD\ of\ control}\right) \times 100$$

Where OD refers to the turbidity values at OD_{660} nm and control refers to the aqueous solution of 1% bovine albumin in distilled water.

5. References

[1] K. Ariga, Q. Ji, M.J. McShane, Y.M. Lvov, A. Vinu, J.P. Hill, Inorganic Nanoarchitectonics for Biological Applications, Chem. Mater. 24 (2012) 728–737.

[2] M.J. Hajipour, K.M. Fromm, A.A. Ashkarran, D. Jimenez de Aberasturi, I.R. de Larramendi, T. Rojo, V. Serpooshan, W.J. Parak, M. Mahmoudi, Antibacterial properties of nanoparticles, Trends Biotechnol. 30 (2012) 499–511.

[3] S. Baker, T. Volova, S.V. Prudnikova, S. Satish, M.N. Nagendra Prasad, Nanoagroparticles emerging trends and future prospect in modern agriculture system, Environ. Toxicol. Pharmacol. 53 (2017) 10–17.

[4] H. Rui, R. Xing, Z. Xu, Y. Hou, S. Goo, S. Sun, Synthesis, functionalization, and biomedical applications of multifunctional magnetic nanoparticles, Adv. Mater. 22 (2010) 2729-2742.

[5] K.D. Gilroy, A. Ruditskiy, H.C. Peng, D. Qin, Y. Xia, Bimetallic Nanocrystals: Syntheses, Properties, and Applications, *Chem. Rev.* 116 (2016) 10414-10472.

[6] M. Khatami, H.Q. Alijani, I. Sharifi, Biosynthesis of bimetallic and core–shellnanoparticles: their biomedical applications –a review, IET Nanobiotechnol. (2018) DOI: 10.1049/iet-nbt.2017.0308.

[7] J.-s. Choi, Y.-w. Jun, S.-I. Yeon, H.C. Kim, J.-S. Shin, J. Cheon, Biocompatible Heterostructured Nanoparticles for Multimodal Biological Detection, J. Am. Chem. Soc. 128 (2006) 15982-15983.

[8] A. Perdikaki, A. Galeou, G. Pilatos, I. Karatasios, N.K. Kanellopoulos, A. Prombona, G.N. Karanikolos, Ag and Cu monometallic and Ag/Cu bimetallic nanoparticle–graphene composites with enhanced antibacterial performance, ACS Appl. Mater. Interfaces 8 (2016) 27498–27510.

[9] O. Antonoglou, K. Giannousi, J. Arvanitidis, S. Mourdikoudis, A. Pantazaki, C. Dendrinou-Samara, Elucidation of one step synthesis of PEGylated CuFe bimetallic nanoparticles. Antimicrobial activity of CuFe@PEG vs Cu@PEG, J. Inorg. Biochem. 177 (2017) 159-170.

[10] O. Antonoglou, J. Moustaka, I.-D. S. Adamakis, I. Sperdouli, A. Pantazaki, M. Moustakas, C. Dendrinou-Samara, Nanobrass CuZn Nanoparticles as Foliar Spray Nonphytotoxic Fungicides, ACS Appl. Mater. Interfaces 10 (2018) 4450−4461.

[11] X. Chen, S. Ku, J. A. Weibel, E. Ximenes, X. Liu, M. Ladisch, S.V. Garimella, Enhanced Antimicrobial Efficacy of Bimetallic Porous CuO Microspheres Decorated with Ag Nanoparticles, ACS Appl. Mater. Interfaces 9 (2017) 39165–39173.

[12] N. Sanpo, C.C. Berndt, C. Wen, J. Wang, Transition metal-substituted cobalt ferrite nanoparticles for biomedical applications, Acta Biomater. 9 (2013) 5830–5837.

[13] N. Sanpo, J. Tharajak, Y. Li, C.C. Berndt, C. Wen, J. Wang, Biocompatibility of transition metal-substituted cobalt ferrite nanoparticles, J. Nanopart. Res. 16 (2014) 2510-2522.

[14] X. Qiu, M. Liu, K. Sunada, M. Miyauchi, K. Hashimoto, A facile one-step hydrothermal synthesis of rhombohedral $CuFeO_2$ crystals with antivirus property, Chem. Commun. 48 (2012) 7365–7367.

[15] Y.-J. Lee, S. Kim, S.-H. Park, H. Park, Y.-D. Huh, Morphology-dependent antibacterial activities of Cu_2O, Mater. Lett. 65 (2011) 818–820.

[16] B. Li, Y. Li, Y. Zhao, L. Sun, Shape-controlled synthesis of Cu_2O nano/microcrystals and their antibacterial activity, J. Phys. Chem. Solids 74 (2013) 1842–1847.

[17] J. Ren, W. Wang, S. Sun, L. Zhang, L. Wang, J. Chang, Crystallography Facet-Dependent Antibacterial Activity: The Case of Cu_2O, Ind. Eng. Chem. Res. 50 (2011) 10366–10369.

[18] K. Giannousi, G. Sarafidis, S. Mourdikoudis, A. Pantazaki, C. Dendrinou-Samara, Selective synthesis of Cu_2O and Cu/Cu_2O NPs: antifungal activity to yeast *Saccharomyces cerevisiae* and DNA interaction, Inorg. Chem. 53 (2014) 9657–9666.

[19] Copper based Nanoparticles as Antimicrobials (Book chapter). K. Giannousi, A. Pantazaki, C. Dendrinou-Samara, Nanostructures for Antimicrobial Therapy: Nanostructures in Therapeutic Medicine Series, Elsevier Inc. 2017, 512-529.

[20] K. Giannousi, K. Lafazanis, J. Arvanitidis, A. Pantazaki, C. Dendrinou-Samara, Hydrothermal synthesis of copper based nanoparticles: Antimicrobial screening and interaction with DNA, J. Inorg. Biochem. 133 (2014) 24–32.

[21] K. Giannousi, M. Menelaou, J. Arvanitidis, M. Angelakeris, A. Pantazaki, C. Dendrinou-Samara, Hetero-nanocomposites of magnetic and antifungal nanoparticles as a platform for magnetomechanical stress induction in *Saccharomyces cerevisiae*, J. Mater. Chem. B 3 (2015) 5341-5351.

[22] N. Lewinski, V. Colvin, R. Drezek, Cytotoxicity of Nanoparticles, Small 4 (2008) 26-49.

[23] P.V. AshaRani, G.L.K. Mun, M.P. Hande, S. Valiyaveettil, Cytotoxicity and Genotoxicity of Silver Nanoparticles in Human Cells, ACS nano 3 (2009) 279-290.

[24] J. Deng , M. Yao , C. Gao, Cytotoxicity of gold nanoparticles with different structures and surface-anchored chiral polymers, Acta Biomater. 53 (2017) 610–618.

[25] M.M. Moharam, M.M. Rashad, E.M. Elsayed, R.M. Abou-Shahba, A facile novel synthesis of delafossite $CuFeO_2$ powders, J Mater Sci: Mater Electron 25 (2014) 1798–1803.

[26] S.P. Pavunny, A. Kumar, R.S. Katiyar, Raman spectroscopy and field emission characterization of delafossite $CuFeO_2$, J. Appl. Phys. 107 (2010) 13522.

[27] Z. Deng, X. Fang, S. Wu, W. Dong, J. Shao, S. Wang, M. Lei, The morphologies and optoelectronic properties of delafossite $CuFeO_2$ thin films prepared by PEG assisted sol–gel method, J. Sol-Gel Sci. Technol. 71 (2014) 297–302.

[28] Y. Yui, Y. Ono, M. Hayashi, J. Nakamura, Synthesis and Electrochemical Properties of $CuFeO_2$ as Negative Electrodes for Sodium-Ion Batteries, American Journal of Physical Chemistry 4 (2015) 16-20.

[29] R.D. Shannon, D.B. Rogers, C.T. Prewitt, Chemistry of noble metal oxides. I. Syntheses and properties of ABO_2 delafossite compounds, Inorg. Chem. 10 (1971) 713–718.

[30] H. Hayashi, Y. Hakuta, Hydrothermal Synthesis of Metal Oxide Nanoparticles in Supercritical Water, Materials 3 (2010) 3794-3817.

[31] M.A. Sarabia, S.D. Rojas, Z. López-Cabaña, R. Villalba, G. González, A.L. Cabrera, Carbon dioxide adsorption studies on delafossite $CuFeO_2$ hydrothermally synthesized, J. Phys. Chem. Solids 98 (2016) 271–279.

[32] X. Zhang, Y. Ding, H. Tang, X. Han, L. Zhu, N. Wang, Degradation of bisphenol A by hydrogen peroxide activated with $CuFeO_2$ microparticles as a heterogeneous Fenton-like catalyst: Efficiency, stability and mechanism, Chem. Eng. J. 236 (2014) 251–262.

[33] J. Gopal, H.N. Abdelhamid, P.-Y. Huaa, H.-F. Wu, Chitosan nanomagnets for effective extraction and sensitive mass spectrometric detection of pathogenic bacterial endotoxin from human urine, J. Mater. Chem. B 1 (2013) 2463.

[34] Y. Jin, G. Chumanov, Solution Synthesis of Pure 2H $CuFeO_2$ at Low Temperatures, RSC Adv. 6 (2016) 26392-26397.

[35] Q. Xu, R. Li, C. Wang, D. Yuan, Visible-light photocatalytic reduction of Cr(VI) using nano-sized delafossite ($CuFeO_2$) synthesized by hydrothermal method, J.Alloys Compd. 723 (2017) 441-447.

[36] J. Lu, X.-T. Li, E.-Q. Ma, L.-P. Mo, Z.-H. Zhang, Superparamagnetic $CuFeO_2$ Nanoparticles in Deep Eutectic Solvent: an Efficient and Recyclable Catalytic System for the Synthesis of Imidazo[1,2 a]pyridines, Chem. Cat. Chem. 6 (2014).

[37] M. Zhu, Y. Wang, D. Meng, X. Qin, G. Dia, Hydrothermal Synthesis of Hematite Nanoparticles and Their Electrochemical Properties, J. Phys. Chem. C 116 (2012) 16276−16285.

[38] C. Caizer, M. Ştefănescu, Synthesis and characterization of copper substituted nickel nano-ferrites by citrate-gel technique, J. Phys. D. Appl. Phys. 35 (2002) 3035–3040.

[39] A.M. Jubb, H.C. Allen, Vibrational Spectroscopic Characterization of Hematite, Maghemite, and Magnetite Thin Films Produced by Vapor Deposition, ACS Appl. Mater. Interfaces 2 (2010) 2804–2812.

[40] H.G.M. Edwards, D.W. Farwell, S.J. Rose, D.N. Smith, Vibrational spectra of copper (II) oxalate dihydrate, $CuC_2O_4 \cdot 2H_2O$, and dipotassium bis-oxalato copper (II) tetrahydrate, $K_2Cu(C_2O_4)_2 \cdot 4H_2O$, J. Mol. Struct. 249 (1991) 233-243.

[41] M.A. Marquardt, N.A. Ashmore, D.P. Cann, Crystal chemistry and electrical properties of the delafossite structure, Thin Solid Films 496 (2006) 146 – 156.

[42] Cuprous oxide (Cu_2O) band structure, band energies (Book chapter). O. Madelung, U. Rössler, M. Schulz, (ed.) Landolt-Börnstein - Group III Condensed Matter 41C (Non-Tetrahedrally Bonded Elements and Binary Compounds I), SpringerMaterials (1998).

[43] J.C. Wang, Cellular roles of DNA topoisomerases: a molecular perspective, Nat. Rev. Mol. Cell. Biol. 3 (2002) 430-440.

[44] J.J. Champoux, DNA topoisomerases: structure, function, and mechanism, Annu. Rev. Biochem. 70 (2001) 369-413.

[45] S.O. Kim, K. Sakchaisri, N.R. Thimmegowda, N.K. Soung, J.H. Jang, Y.S. Kim, K.S. Lee, Y.T. Kwon, Y. Asami, J.S. Ahn, R.L. Erikson, B.Y. Kim, STK295900, a Dual Inhibitor of Topoisomerase 1 and 2, Induces G_2 Arrest in the Absence of DNA Damage, PLoS One 8 (2003) 53908.

[46] D. Battal, A. Çelik, G. Güler, A. Aktaş, S. Yildirimcan, K. Ocakoglu, Ü. Çömelekoğlu, SiO_2 Nanoparticule-induced size-dependent genotoxicity – an in vitro study using sister chromatid exchange, micronucleus and comet assay, Drug Chem. Toxicol. 38 (2015) 196-204.

[47] A.L. Di Virgilio, M. Reigosa, P.M. Arnal, M. Fernαndez Lorenzo de Mele, Comparative study of the cytotoxic and genotoxic effects of titanium oxide and aluminium oxide nanoparticles in Chinese hamster ovary (CHO-K1) cells, J. Hazard. Mater. 177 (2010) 711-718.

[48] A. Nomani , X. Chen , A. Hatefi, Evaluation of genotoxicity and mutagenic effects of vector/DNA nanocomplexes in transfected mesenchymal stem cells by flow cytometry, Acta Biomater. 74 (2018) 236–246.

[49] H. Turkez, M.I. Yousef, E. Sönmez, B. Togar, F. Bakan, P. Sozio, A. Di Stefano, Evaluation of cytotoxic, oxidative stress and genotoxic responses of hydroxyapatite nanoparticles on human blood cells, J. Appl. Toxicol. 34 (2014) 373-379.

[50] E. Andreadou, A. Moschopoulou, O. Simou, T. Lialiaris, A. Pantazaki, *T. thermophilus* Rhamnolipids Induce Cytogenetic Damage on Human Lymphocytes and Bind DNA *in vitro*, Br. Biotechnol. J. 10 (2016) 1-12.

[51] T. Lialiaris, D. Mourelatos, L. Boutis, A. Papageorgiou, M. Christianopoulou, V. Papageorgiou, J. Dozi-Vassiliades, Comparative study on cytogenetic effects by diplatinum complexes of the ligands of naphthazarine and squaric acid in human lymphocytes, J. Pharmacol. Exp. Ther. 251 (1989) 368–371.

[52] E. Sonoda, M.S. Sasaki, C. Morrison, Y. Yamaguchi-Iwai, M. Takata, S. Takeda, Sister chromatid exchanges are mediated by homologous recombination in vertebrate cells. Mol Cell Biol. 19 (1999) 5166-5169.

[53] R.D. Johnson, M. Jasin, Sister chromatid gene conversion is a prominent double-strand break repair pathway in mammalian cells, EMBO J. 19 (2000) 3398-3407.

[54] E. Mylonaki-Charalambours, D. Mourelatos, A. Kotsis, A comparative study of the cytogenetic and antineoplasmatic effects induced by carboplatin in combination with niacin in human lymphocytes in vitro and in Ehrlich ascites tumor cells in vivo, Chemotherapy 44 (1998) 121-128.

[55] A. Kourakis, J. Dozi-Vassiliades, P. Hatzitheodoridou, J. Tsiouris, D. Mourelatos, Practical applications of the SCE studies for guiding and improving chemotherapy, Basic Life Sci. 29 (1984) 907-914.

[56] H. Neurath, J.P. Greenstein, F.W. Putnam, J.O. Erickson, The chemistry of protein denaturation, Chem. Rev. 34 (1944) 157-265.

[57] S.S. Ali, R. Morsy, N.A. El-Zawawy, M.F. Fareed, M.Y. Bedaiwy, Synthesized zinc peroxide nanoparticles (ZnO_2-NPs): a novel antimicrobial, anti-elastase, anti-keratinase, and anti-inflammatory approach toward polymicrobial burn wounds, Int. J. Nanomed. 12 (2017) 6059–6073.

[58] I. Gnanasundaram, K. Balakrishnan, Synthesis and Evaluation of Anti-Inflammatory Activity of Silver Nanoparticles from *Cissus vitiginea* Leaf Extract, J. Nanosci. Nanotechnol. 3 (2017) 266-269.

[59] H. Abdulalsalam, N.M. Ardalan, S.H. Ahmed, Evaluation of anti-inflammatory effect by using iron nanoparticles prepared by *Juglans regia* water extract, Curr Res Microbiol Biotechnol. 5 (2017)1151-1156.

[60] G. Kishore, G. Siva, E.S. Sindhu, *In Vitro* Anti-Inflammatory and Anti-Arthritic Activity of Leaves of Physalis Angulata L, Int. J. Pharmacetical Ind. Res. 1 (2012) 211–213.

[61] T. Lialiaris, E. Kotsiou, S. Pouliliou, D. Kareli, H. Makrinou, A. Kouskoukis, F. Papachristou, M. Koukourakis, Cytoprotective activity of amifostine on cultured human lymphocytes exposed to irinotecan, Food Chem. Toxicol. 47 (2009) 2445-2449.

[62] E. Digkas, D. Kareli, S. Chrisafi, T. Passadaki, E. Mantadakis, A. Hatzimichail, V. Vargemezis, T. Lialiaris, Attenuation of cytogenetic effects by erythropoietin in human lymphocytes in vitro and P388 ascites tumor cells in vivo treated with irinotecan (CPT-11), Food Chem. Toxicol. 48 (2010) 242-249.

[63] T. Lialiaris, A. Pantazaki, E. Sivridis, D. Mourelatos, Chloropromazine- induced damage on nucleic acids: A combined cytogenetic and biochemical study, Mutat. Res. 265 (1992) 155-163.

[64] E.N. Digkas, S. Chrisafi, T. Passadaki, A. Tsalkidis, A. Hatzimichail, V. Vargemezis, T. Lialiaris, *In vitro* and *in vivo* cytogenetic effects of recombinant human erythropoietin on the frequency of sister chromatid exchanges alone or in combination with mitomycin C, Chemotherapy 56 (2010) 239-247.

[65] T. Lialiaris, P. Mavromatidou, E. Digkas, T. Passadaki, P. Mpountoukas, S. Panagoutsos, V. Vargemezis, Chromosome instability in patients with chronic renal failure, Genet. Test. Mol. Biomarkers. 14 (2010) 37-41.

[66] T. Morris, M. Stables, A. Hobbs, P. de Souza, P. Colville-Nash, T. Warner, J. Newson, G. Bellingan, D.W. Gilroy, Effects of low-dose aspirin on acute inflammatory responses in humans, J. Immunol. 183 (2009) 2089–2096.

[67] S. Sakat, A. Juvekar, M. Gambhire, In vitro antioxidant and anti-inflammatory activity of methanol extract of *Oxalis corniculata* Linn, Int. J. Pharm. Sci. 2 (2010) 146–155.
[68] M. Catauro, E. Tranquillo, G. Dal Poggetto, M. Pasquali, A. Dell'Era, S. Vecchio Ciprioti, Influence of the heat treatment on the particles size and on the crystalline phase of TiO_2 synthesized by the sol-gel method, Materials 11 (2018) 2364.
[69] M. Catauro, E. Tranquillo, F. Barrino, I. Blanco, F. Dal Poggetto, D. Naviglio, Drug release of hybrid materials containing Fe(II)citrate synthesized by sol-gel technique, Materials 11 (2018) 2270.